



ELSEVIER

Contents lists available at ScienceDirect

Optics Communications

journal homepage: www.elsevier.com/locate/optcom

Integration of high transmittance photonic crystal H2 nanocavity and broadband W1 waveguide for biosensing applications based on Silicon-on-Insulator substrate

Jian Zhou^a, Huiping Tian^{a,*}, Daquan Yang^{a,b}, Qi Liu^a, Yuefeng Ji^a

^a The State Key Laboratory of Information Photonics and Optical Communications, School of Information and Communication Engineering, Beijing University of Posts and Telecommunications, Beijing 100876, China

^b School of Engineering and Applied Sciences, Harvard University, Cambridge, MA 02138, USA

ARTICLE INFO

Article history:

Received 18 March 2014

Received in revised form

26 April 2014

Accepted 28 April 2014

Keywords:

Photonic crystal

Biosensor

Nanocavity

Waveguide

SOI

ABSTRACT

In this paper, we exhibit an integration of simultaneously high transmittance and high extinction ratio H2-type photonic crystal (PhC) nanocavity and broadband W1 waveguide above Silicon-on-Insulator (SOI) substrate. The integrated structure can be used as an opto-fluidic architecture for label-free biochemical detection with high resolution and large sensing range. With the plane-wave expansion (PWE) method, the results show a single resonant mode operation at normalized frequency between 0.2213 ($2\pi c/a$) and 0.2917 ($2\pi c/a$), which correspond to wide resonant wavelength ranges from 1440 to 1898 nm. By applying three-dimensional finite-difference time-domain (3D-FDTD) technique, we simulate the change of optical properties caused by the H2 structural variation. Through modifying the number and sizes of the air-holes near to the defect cavity, over 95% transmission efficiency is achieved, accompanied with an improved extinction ratio of 25 dB. Combined broadband W1 waveguide with high transmittance H2 nanocavity well meets the demand of extensive biosensing. In addition, a high resolution that we show to be $O(10^{-6})$ refractive index units (RIU) under optimal conditions.

© 2014 Published by Elsevier B.V.

1. Introduction

Recently, optical techniques have been very attractive for performing sensitive and label-free biomolecular detection since they are easily penetrated in fluid cells containing the analyte. Compared with analogous mechanical or electrical label free methods [1], the major superiorities of these techniques are that the devices can be relatively easy to manufacture and the wide range of fluids where they can be measured (e.g. gas, water and solution, etc.). The detection principle is based on the change in refractive index (reflected by a change in the wavelength of the resonant peak) experienced by the electromagnetic field near the surface with the presence of the target molecules, so that the target does not require any fluorescent labeling. Sensors-based label-free detections are especially fascinating, not only just because they avoid expensive and complex labeling procedures, but also because the labels may influence the biomolecule recognition and the small interrogation volume makes them more sensitive to extensive properties (e.g. bulk sensitivity). But there

exists a main limitation to be integrated in optical chips at a large sensing area ($\sim \text{mm}^2$).

Due to the development of photonic crystals [2–3], miniaturization of optical sensors has been realized. In addition, many efforts were made to achieve nano-scale devices such as photonic crystal (PhC) fibers [1] and PhC cavities [4–17]. Because of the small mode volume, the total measurable change in the refraction index can also be very small. Examples of such systems include that of Ouerghi et al. [18] who demonstrated a theoretical study on a novel chemical sensor platform based on a 2-D photonic crystal with negative refraction (PCNR), Larqué et al. [19] who demonstrated a theoretical investigation of photonic crystal cavities etched on a suspended membrane for the generation of polarization entangled photon pairs using the biexciton cascade in a single quantum dot, Dominguez-Juarez et al. [20] who demonstrated that using high-Q spherical micro-resonators and low average power, between 50 and 100 small non-fluorescent molecules deposited on the outer surface of the micro-resonator can generate a detectable change in the second harmonic light. However, the drawback of these designs is that they display a low transmittance (about 80%) and extinction ratio, which may have a strong impact on detection properties. In order to overcome this drawback and realize more precise sensing effect, high-transmission-based sensor using photonic crystal has been developed. Examples of such

* Correspondence to: Beijing University of Posts and Telecommunications, P.O.BOX 90, #10 Xitucheng Road Haidian District, Beijing 100876, China. Tel.: +86 10 62282153.

E-mail addresses: hptian@bupt.edu.cn (H. Tian), jyf@bupt.edu.cn (Y. Ji).

<http://dx.doi.org/10.1016/j.optcom.2014.04.075>

0030-4018/© 2014 Published by Elsevier B.V.

systems include that of Alivisatos et al. [21] who demonstrated new systems that will be capable of sensing at the single-molecule level in living cells, and capable of parallel integration for detection of multiple signals, enabling a diversity of simultaneous experiments, as well as better crosschecks and controls, Kurt et al. [22] who demonstrated a new bio-sensor concept that incorporates photonic crystal (PC) surface modes to sense small refractive index changes, and Dündar et al. [23] who demonstrated an InAs quantum dot-embedded PhC membrane nanocavity for sensing application. However, in the Ref. [21–23], all which present high transmittance, but a low quality (Q) factor (about 400–500) in the Refs. [21,22], while the extinction ratio of single drop of nanocavity in the Ref. [23] is only 8–10 dB.

In this work, we present an integration of simultaneously high transmittance and high extinction ratio H2-type photonic crystal (PhC) nanocavity and broadband W1 waveguide based on Silicon-on-Insulator (SOI) substrate. The simulation results demonstrate that a wide range between 0.2213 ($2\pi c/a$) and 0.2917 ($2\pi c/a$) is obtained. Thus we can observe that a large bandwidth ranges from 1440 to 1898 nm. Compared with the Ref. [15] in which the resonant wavelength ranges only from 1481.7 to 1748.9 nm. In addition, by shrinking the second to third closest neighbor holes in the $\Gamma-K$ direction around the defect, we demonstrate that transmittance can be improved to over 95%, while extinction ratio exceeding 25 dB. Remarkably, under different optimized parameters, we also calculate the Q factors of modification exceeding 2966. This high quality attributes to the couple between the broadband W1 waveguide and high transmittance H2 PhC nanocavity. Based on the combination of broad W1 waveguide and H2 nanocavity, this device is well fit to biosensing with extensive range and high resolution. Indeed, the numerical simulations reveal that the relationship between resonant wavelength shifts and the refractive index changes is linear in the refractive index range. In the case of the number of functionalized holes equals 14 ($N=14$), the sensitivity of 131.70 nm/RIU is obtained and a high refractive index detection limit is approximately of 3.797×10^{-6} for this device. Through modifying the number of functionalized holes, the sensitivity can also be adjusted from 75.08 nm/RIU (when $N=2$) to 150.15 nm/RIU (when $N=42$).

2. The design of broadband W1 waveguide and high transmittance H2 PhC nanocavity

2.1. The design of broadband W1 waveguide

Fig. 1 shows a 3D schematic diagram of our PhCW structure design which is based on triangular lattice, hole-array based PhC slab. It is constructed in a silicon slab ($n_{\text{Si}}=3.4$) by arranging a triangular lattice of air holes on SOI substrate, where the central row of air holes is removed in order to form a line defect waveguide (W1). Compared with square lattice PhC, a triangular lattice can be a great advantage to acquire a wider PBG. With regard to the pillar-array PhC, hole-array with a strong refractive-index contrast is easier to form a suspended free-standing membrane. Based on this system, the defect mode may lie partly below the cladding light line in the $k-\omega$ plane [25,26]. In this case the mode is truly guided with no intrinsic diffraction loss (unlike modes above the light line which are subject to intrinsic out-of-plane losses). Therefore in order to obtain a W1 waveguide with large bandwidth and small vertical loss, the structure design in this paper is based on triangular lattice, hole-array based PhC (Fig. 1). In this paper, the plane wave expansion (PWE) method and the open source FDTD software Meep are used to calculate their photonic band structure and transmission spectra, respectively [27]. We set the light source at the head of the input W1

waveguide and monitor is located at the end of the output W1 waveguide. In our simulations, we set this resolution to 20 (namely, with a grid spacing of $a/20$, where a is the lattice constant) and all the simulations are implemented at the same resolution ($=20$) in order to obtain consistent comparison results.

Fig. 1 shows that the W1 PhC slab waveguide is patterned by a PhC single line defect waveguide with a triangular lattice of air holes. The diameter of air hole is 268.8 nm and the lattice constant is $a=420$ nm. The thickness of PhC slab waveguide is $T=0.578a=242.8$ nm.

A typical band diagram for TE-like polarized light of the W1 PhC is simulated numerically by the PWE method which is displayed in Fig. 2(a). Both even and odd modes are showed between air and dielectric mode. In the slab waveguide, the modes which lie above the light line will exhibit high intrinsic loss in the z -direction. In addition, only the even TE slab modes will be coupled to the waveguide or resonators in the 2D photonic crystal slab sensor structure, while the odd modes will be leaked out in the same design. For this reason we focus on the designing defects that support even modes [28,29]. Thus, the even mode is regarded as the guided mode. In Fig. 2(a), the gap of the even mode is around 0.2156–0.2923 ($2\pi c/a$), and the transmission is in the range 0.2213–0.2917 ($2\pi c/a$) in Fig. 2(b). The guided modes are lying below the light line of the air, which are intrinsically lossless in the vertical direction. The guided band edge refers to the cutoff frequency of the guided mode. And the up and bottom edge correspond to the highest and lowest frequency for PBG, respectively. And PBG is shown as like Fig. 2(b), in addition, a wide band is between 0.2213 ($2\pi c/a$) and 0.2917 ($2\pi c/a$). Thus the corresponding broad wavelength range is between 1440 and 1898 nm. However, in the Refs. [15] and [30], the available bandwidth is only 200 and 86 nm, respectively. Therefore this sufficient broadband can meet the demand the sensing that the resonant mode produces a wide range of wavelength shift.

With reasonable design about the structure parameters, the strong index contrast produces total internal reflection (TIR) (which occurs at a boundary separating materials with different refractive indices) in the Z (out of plane) direction. PhC slab waveguide has truly guided modes which do not exhibit out-of-plane radiation loss. Propagation of light in this structure is well controlled by the dielectric discontinuity of the slab in the vertical direction. Meanwhile, due to a combination of 2D PBG (Fig. 2(b)) and 1D TIR, the TE-like polarized light is strongly confined in both in-plane direction (Fig. 3(a)) and out-plane (Fig. 3(b)) direction. Just as Fig. 3, both in horizontal direction and vertical direction, the leakage of light becomes very small. Finally, the properties of a wide band (Fig. 2) and well confinement of light (Fig. 3) are better applied into the biosensor design Fig. 4.

2.2. The high transmittance H2 PhC nanocavity design based on above broadband W1 waveguide

In practice, a 2D photonic crystal slab has emerged as one of the most important platforms to design a high transmission and high quality factor (Q) optical microcavity. The presence of a microcavity in the periodicity creates a transmission resonance in the band gap associated with a trapped state. Then we hope that light at wavelengths near a resonance is largely transmitted and obtain high transmittance as much as possible, such as plasmonic nanocavity [31]. Small cavities with a high Q can enhance various light-matter interactions. This enhancement can be applied to improve the performance of various optical devices. Extensive studies have continued with the aim of realizing smaller cavities with higher Q factors, such as Ln cavity [32,33], Quantum-dot cavity [35] and H1 cavity [36]. Due to the dependence of the resonance mode on the defect size of nanocavity [37], the PhC cavity size should be selected

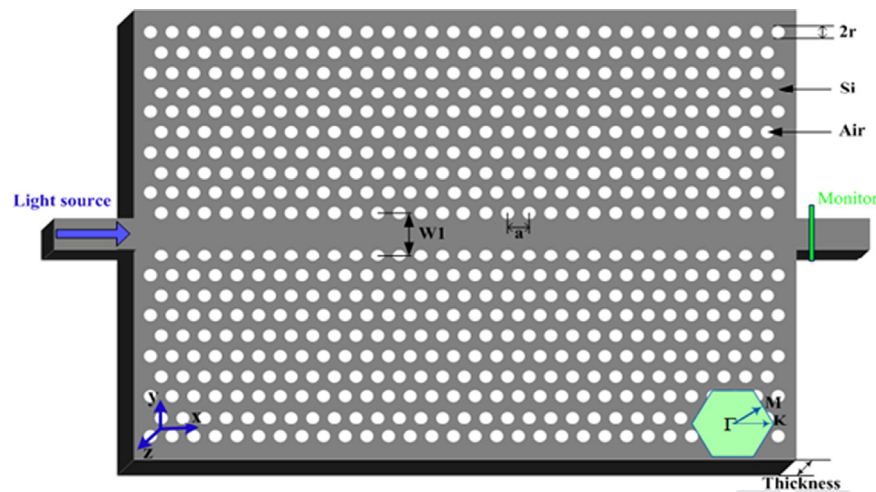


Fig. 1. Schematic diagram of the 3D W1 PhC slab waveguide, with air hole radius $r=0.32a$, a triangular lattice constant $a=450$ nm and slab thickness $T=0.578a$.

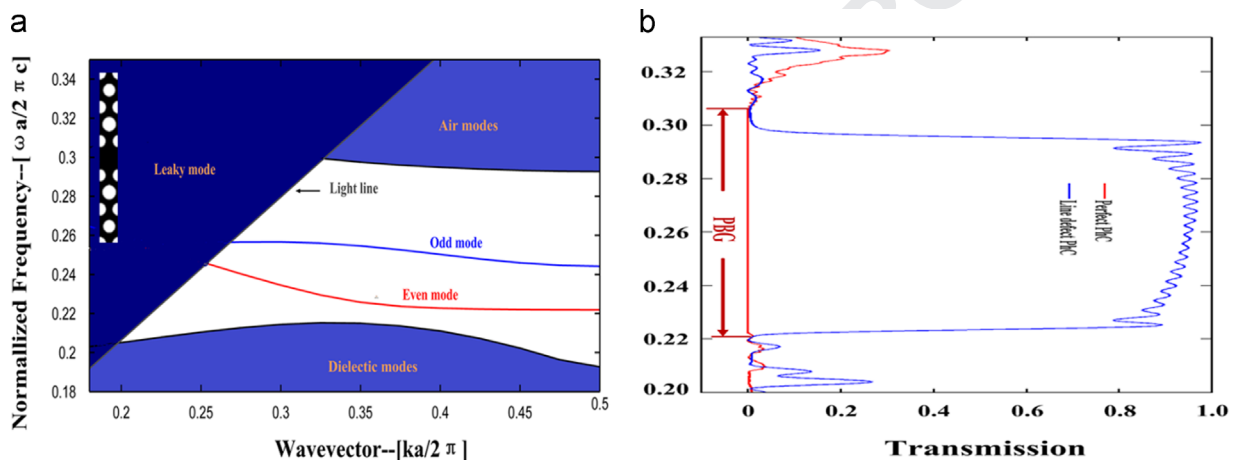


Fig. 2. (a) A typical band diagram of broadband W1 PhC slab; (b) The transmission spectrum of perfect PhC (red solid line) and line defect PhC (blue solid line). (For interpretation of the references to color in this figure legend, the reader is referred to the web version of this article).

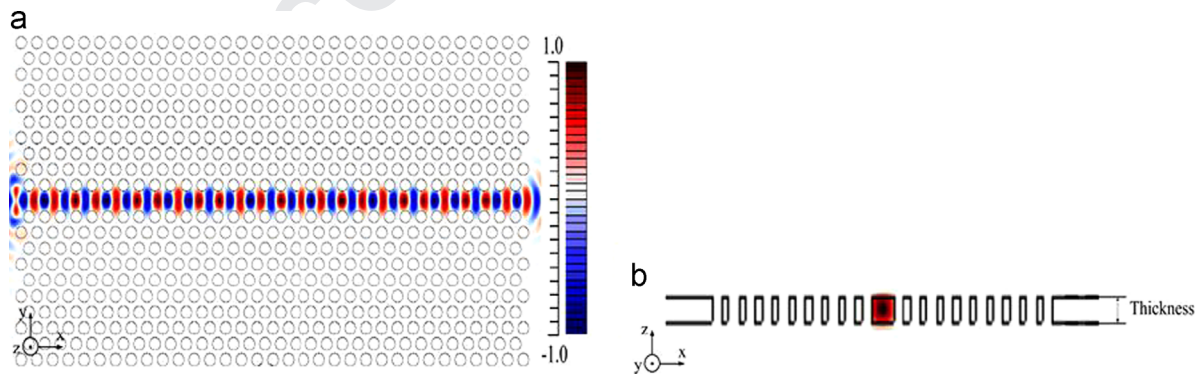


Fig. 3. Electric field distribution of W1 PhC slab by Meep simulations in (a) x - y plane and (b) x - z plane.

carefully in order to realize the high quality, sensitivity and the wide measure range. Meanwhile, the higher transmission efficiency and extinction ratio can be obtained by optimizing the air holes parameters around the defect. In this paper, based on the broadband W1 waveguide structure mentioned above, we increase the transmission and Q -factor of our device which is further designed by three factors: changing the length of the defect (L), shrinking the radius r_1 of green air holes, and adjusting the radius r_2 of red air holes. However, if we want to excite the cavity mode directly, then the energy in the cavity would leak out slowly [24]. Something

more interesting happens when we excite the cavity from the waveguide, the detected spectrum has a Lorentzian line shape and peak intensity occurs at resonance. Thereby it provides a better coupling between the W1 waveguide and the nanocavity for improving the Q factor.

The defect length is scanned to optimize the quality of the fundamental cavity mode, as shown in Fig. 5(a). The defect length ($L=2$) results in an optimal design at $(\omega=0.257(2\pi c/a))$ with a Q factor of 814. The Q factor is defined as $\lambda_0/\Delta\lambda$, where λ_0 is the resonance wavelength and $\Delta\lambda$ is the FWHM of the resonator's

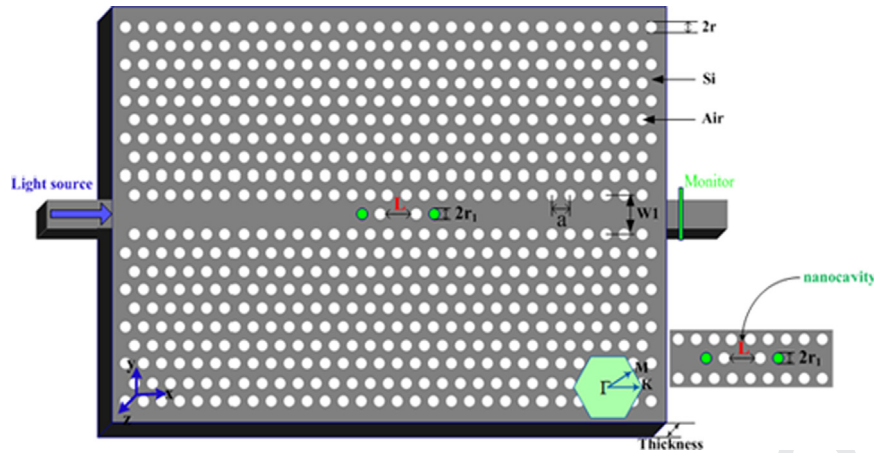


Fig. 4. Schematic diagram of the nanocavity based on the broadband W1 waveguide. The nanocavity can be formed by varying the length (L) of the defect, where $a=450$ nm, $r=0.32a$, $T=0.578a$.

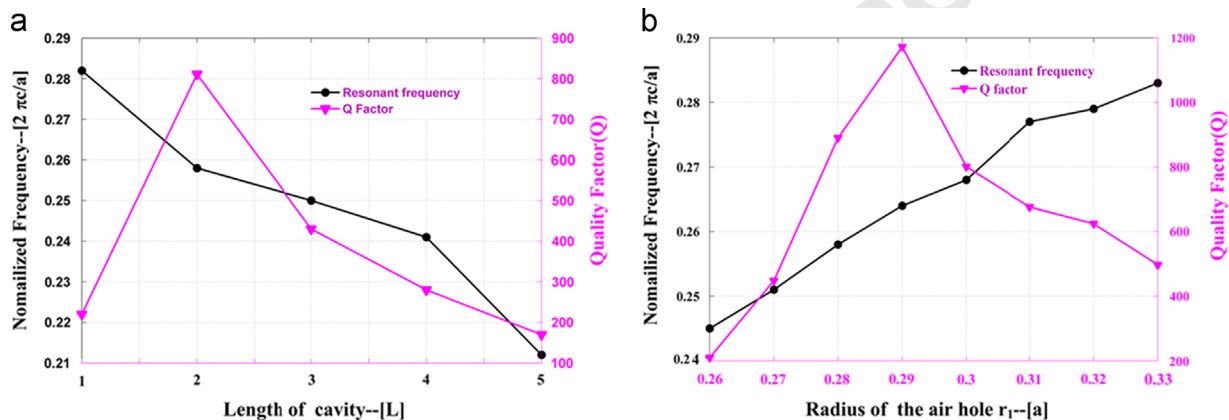


Fig. 5. Result of FDTD calculations displaying the cavity resonance frequencies and quality factors Q as a function of (a) the defect (L) and (b) the air hole radius r_1 based on the length of defect ($L=2$).

Lorentzian response. This value compares favorably with those of previous works [21,22]. As the defect becomes longer, the resonance is pushed to lower frequencies (the resonance wavelength should redshift due to the increase in the effective index of the cavity [see in Fig. 5(a)]), which the theoretical results agreed with the simulated calculations.

In H2 cavity structure, the radius of air hole could be optimized to achieve the high- Q factor and transmission efficiency simultaneously. The FDTD method can be used to calculate the transmission and the Q factor when the green air hole radius (r_1) are scanned from $0.26a$ to $0.33a$ based on the defect length ($L=2$) as showed in Fig. 5(b). When the radius of air hole (r_1) is increased, the cavity resonance shifts towards higher frequencies. As seen in Fig. 5(b), the air hole radius of $r_1=0.29a$ leads to an optimal design with a Q factor of 1176.

Fig. 6(a) shows the theoretical results of transmittance in terms of air hole (r_1) based on H2 nanocavity. The optimum result appears at $r_1=0.29a$ that the transmission efficiency reaches 90.5%. A sharp peak appears inside the complete bandgap in TE Polarization of the PC at the resonance frequency of the cavity ($L=1$) in Fig. 6(b). Gaussian light source is transmitted for frequencies near the resonance frequency of the cavity. The existence of the resonance peak shows the waveguide can couple with the cavity. Then the calculated Q factor value for this resonance is about 300 (Fig. 5(a)). The extinction ratio reached 30 dB while the transmittance was very low (only about 60%). Compared with Fig. 6(a and b) shows a rapid improvement in the transmittance.

In order to further obtain higher Q factor and transmission efficiency, a new air hole is added around the H2 cavity (Fig. 7). It can be also noted that the Q factor will be enhanced when the wall of the cavity is increasing [36]. Therefore, the Q factor improvement is attributed to the effect of the air hole. Whilst shrinking the radius of red air hole can reduce unwanted reflection. Fig. 8(a) shows that an air hole radius $r_2=0.18a$ results in an optimal design based on H2 cavity and $r_1=0.29a$ with a Q factor of 2966. As expected, the cavity resonance is pushed to higher frequencies when the radius of air hole r_2 is enlarged. The transmission efficiency is as a function of r_2 showing in Fig. 8(b), over 95% transmittance is observed when the air hole $r_2=0.18a$ and a plot of the optimum transmission spectra in Fig. 6(c). However, the extinction ratio presents a slightly degeneracy (down to 25 dB).

Fig. 9(a) shows that the electric field distribution is not well focused on the H2 cavity when a Gaussian light source is located in the center of H2 cavity. When we continuously design new parameters (r_2) for optimizing the H2 cavity and enhance the local effect for the field distribution. As plotted in Fig. 9(b), we can observe that the optimized H2 cavity has a strong optical local field. Due to the large degree of light-matter interaction, it leads the H2 PhC nanocavity to be sensitive to tiny refractive index changes.

3. Sensing properties for the designed structure

For applications such as bio-sensing or chemical detection, it is important to note that the device does not measure variations in

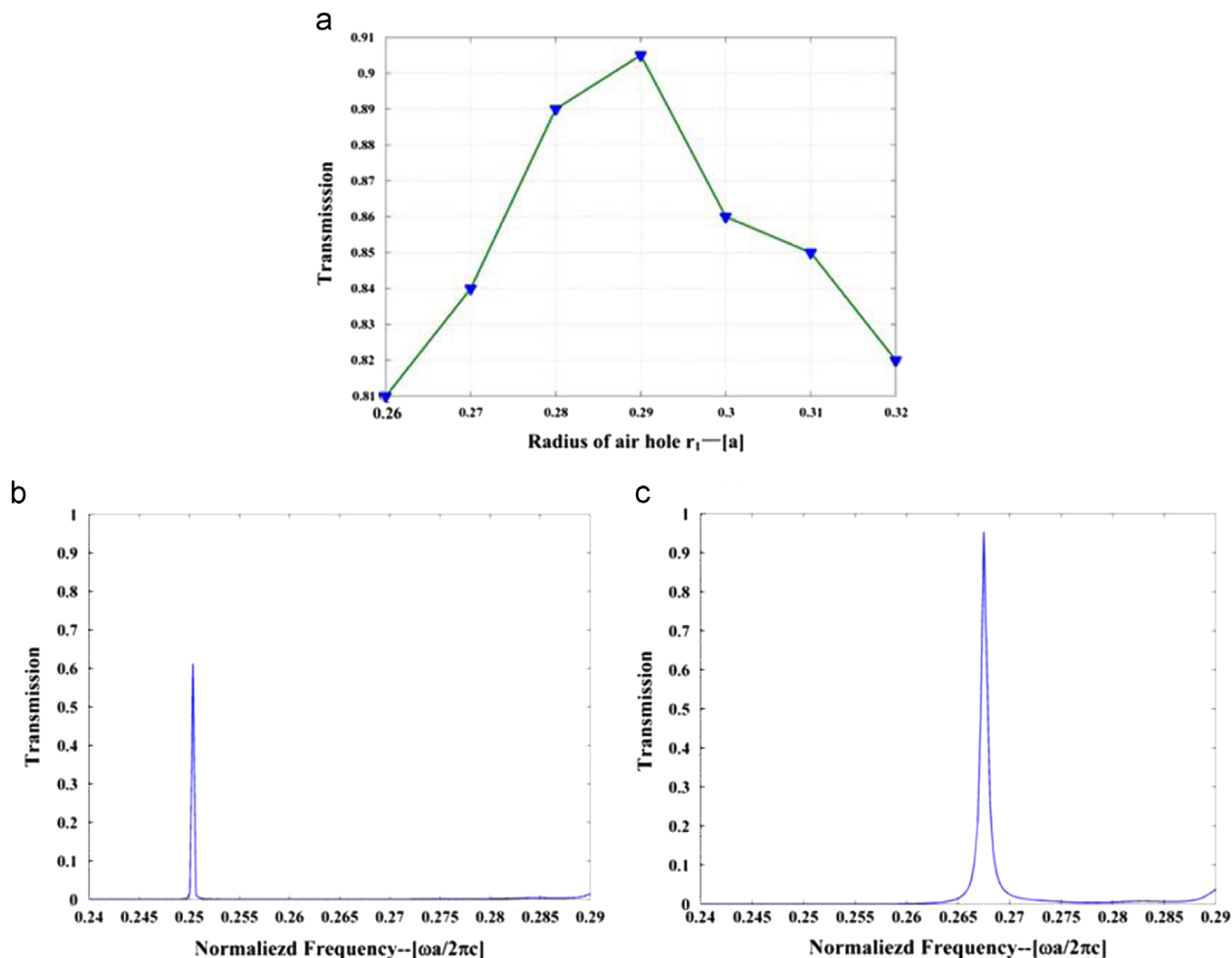


Fig. 6. (a) Result of FDTD calculations showing transmittance as a function of r_1 based on H2 cavity, (b) output transmission spectra for cavity ($L=1$) and (c) transmission spectra for the H2 nanocavity based on the air hole radius $r_1=0.29a$ and the defect length ($L=2$).

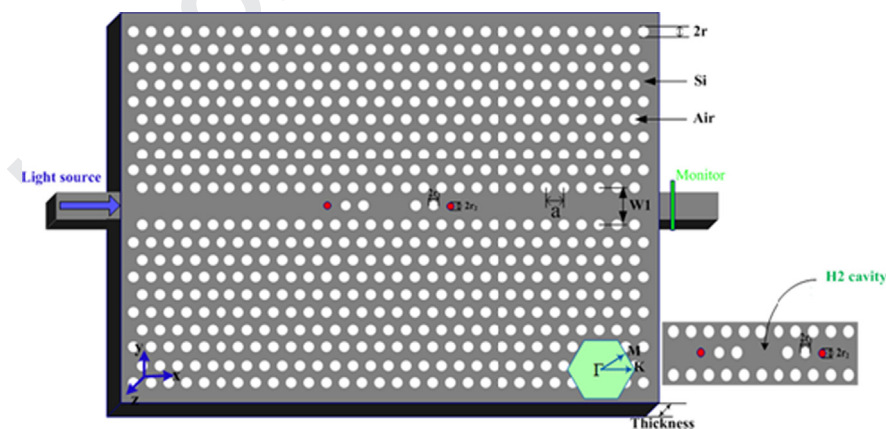


Fig. 7. Schematic diagram of the integration of high transmittance H2 PhC nanocavity and the broadband W1 waveguide, where $r_1=0.29a$, $a=450$ nm, $r=0.32a$ and $T=0.578a$.

the bulk refractive index of the surrounding medium, but rather respond to the local variations in refractive index in the area of the individual sensor. Therefore, the magnitude of the resonant shift will rely on the effective refractive index change of targets. To construct this model, we performed the detailed 3D-FDTD simulations wherein we studied the sensitivity of this sensor design and demanded how to achieve the lowest mass limit of detection. For example, the refractive index surrounding the cavity changes when a kind of target object was filled into the air holes around

the resonant cavity. The refractive index change surrounding the resonant cavity results from the detected targets object bind with pre-existing complimentary probes. The molecular of the sugar-water was used in our simulations. We varied the number of holes around the H2 cavity being functionalized to study the mass sensitivity of the structure as a function of the number of functionalized holes. Simulations were performed for the conditions of two holes (the innermost holes on the either side of the H2 cavity), four holes (the innermost holes on either side of the

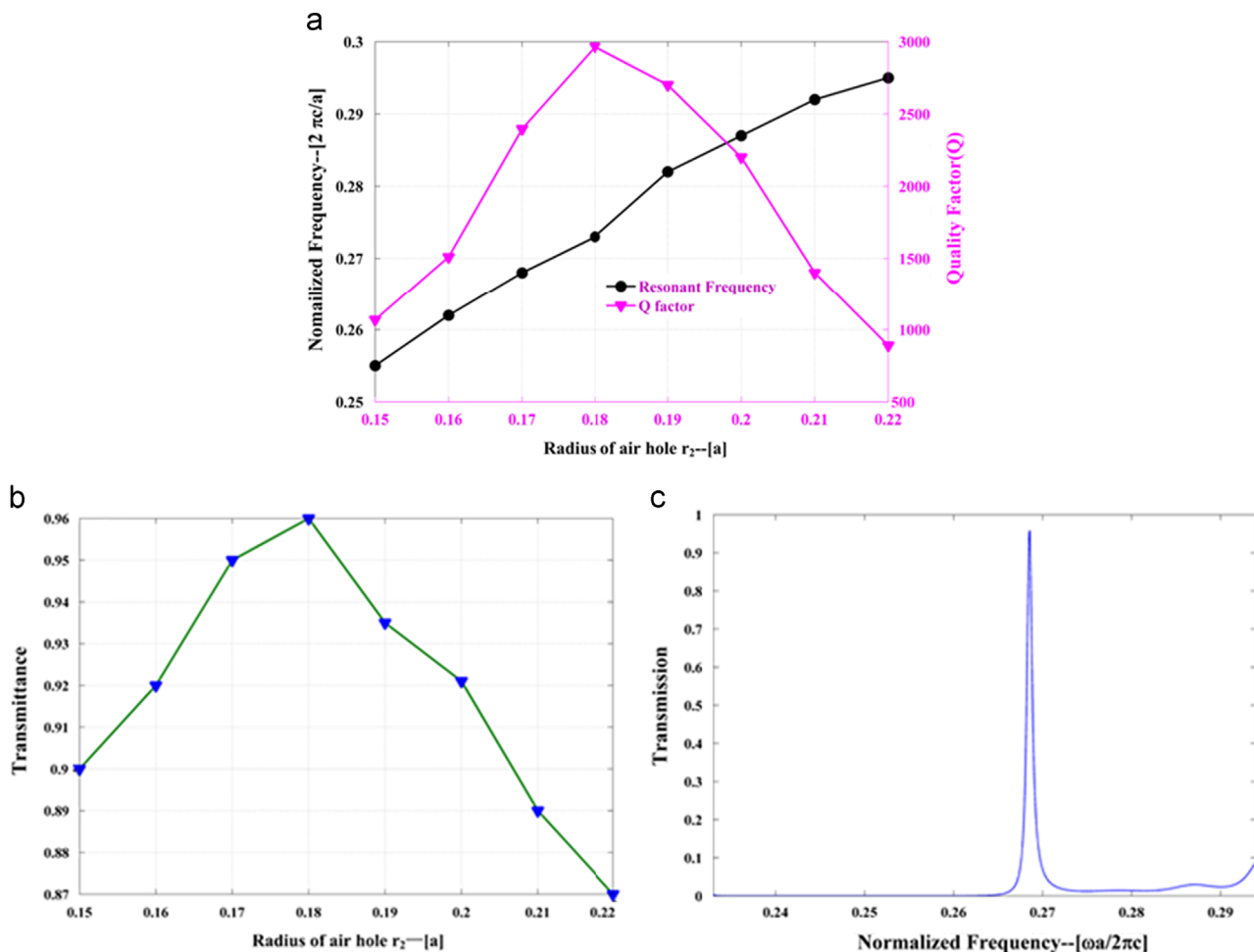


Fig. 8. (a) Result of FDTD calculations showing the H2 cavity resonance frequencies and the quality factors as a function the air hole radius r_2 based on $r_1 = 0.29a$; (b) transmittance as a function of r_2 based on H2 cavity and $r_1 = 0.29a$ and (c) the output transmission spectra based on H2 cavity, where the air hole radius $r_2 = 0.18a$ and $r_1 = 0.29a$.

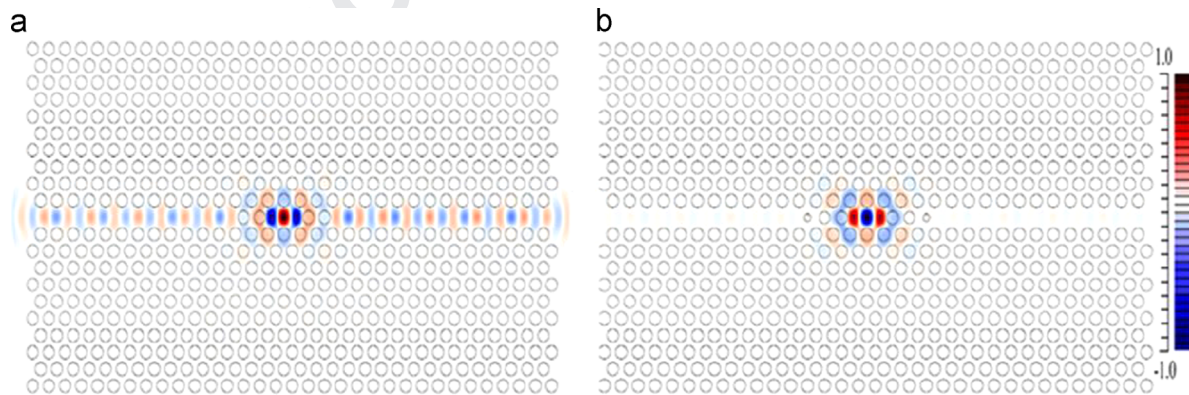


Fig. 9. The intensity field distribution in the x-y plane for the H2 cavity based on (a) the air hole $r_1 = 0.29a$ and (b) the air hole radius $r_1 = 0.29a$ and $r_2 = 0.18a$. A Gaussian light source is located in the centre of H2 PhC nanocavity.

cavity and the innermost holes on the top and bottom side of the H2 cavity), and so forth, up to 42 holes (three holes on either side and eighteen holes on top and bottom edge) being functionalized. We have calculated the term $\Delta\lambda/N$ in all cases where $\Delta\lambda$ is the shift in the resonant wavelength of the design structure and N is number of the functionalized holes. The $\Delta\lambda/N$ is defined as the mass sensitivity of this structure. In this situation, we use sugar-water molecules as our model species due to the availability of data relating the change in the local refractive index with the surface concentration of bound targets.

Table 1 shows that mass sensitivity ($\Delta\lambda/N$) and resonant wavelength shift ($\Delta\lambda$) when number of functionalized holes (N) changes. Meanwhile the constant concentration of sugar-water is infiltrated into the functionalized holes. As can be seen, the innermost are the most sensitive to any refractive index changes in the local environment, on the contrary, the holes that are further away from the resonant cavity. These results can be explained by noting that in Fig. 9(b) the evanescent field is strongest inside the innermost holes and decreases inside holes that are located further away from the cavity. It is very important

to note because targeting only the inner most holes for functionalization takes into consideration the lowest possible limit of mass detection for this device.

Fig. 10 is a plot illustrating the dependence of mass sensitivity ($\Delta\lambda/N$) and resonant wavelength shift ($\Delta\lambda$) on the number of functionalized holes (N). We can observe that an exponential function of the form $k_1e^{k_2N} + k_3e^{k_4N}$ (shown in red) in Fig. 10(a), where k_1 , k_2 , k_3 , and k_4 are arbitrary constants approximates this dependency quite well. Thus allowing for all of the above we can express the mass sensitivity as follows:

$$\frac{\Delta\lambda}{N} = \frac{k_1e^{k_2N} + k_3e^{k_4N}}{N} \quad (1)$$

where k_1 , k_2 , k_3 , and k_4 are arbitrary constants, from Eq. (1) we can observe if we lower the number of the holes, the mass sensitivity increases. Eq. (1) is used to fit the purple curve in Fig. 10(a) where the values k_1 , k_2 , k_3 , and k_4 are 5.7120, -0.0402 , 17.6727, and -0.4480 , respectively. The regression coefficient R can be expressed Eq. (2) as follows:

$$R^2 = \frac{\sum (Y - \bar{Y})^2}{\sum (Y_j - \bar{Y})^2} \quad (2)$$

where Y is the fitted value of the regression curve, \bar{Y} is the mean value of the simulation and Y_j is the calculated value. The regression coefficient is 0.9998. Thus, this analytical expression shows good agreement with the FDTD simulation results and helps us to understand that the mass sensitivity of the device increases with a decrease in the number of the functionalized holes. However, Fig. 10(b) reveals that the resonant wavelength is positive proportion to the number of functionalized holes, and the point of $N=14$ can be seen as a demarcation point. As seen in Fig. 10(a), the sensing element can realize higher mass sensitivity ($N=2, 4$ and 8), but the refractive index sensitivity is lower (Fig. 10(a)); on the contrary the

Table 1

Mass sensitivity ($\Delta\lambda/N$) and resonant wavelength shift ($\Delta\lambda$) with different number of functionalized holes (N).

N	0	2	4	8	14	20	32	42
$\Delta\lambda$	0	25	31	38	44	47	49	50
$\Delta\lambda/N$		12.5	7.75	4.75	3.14	2.35	1.53	1.19

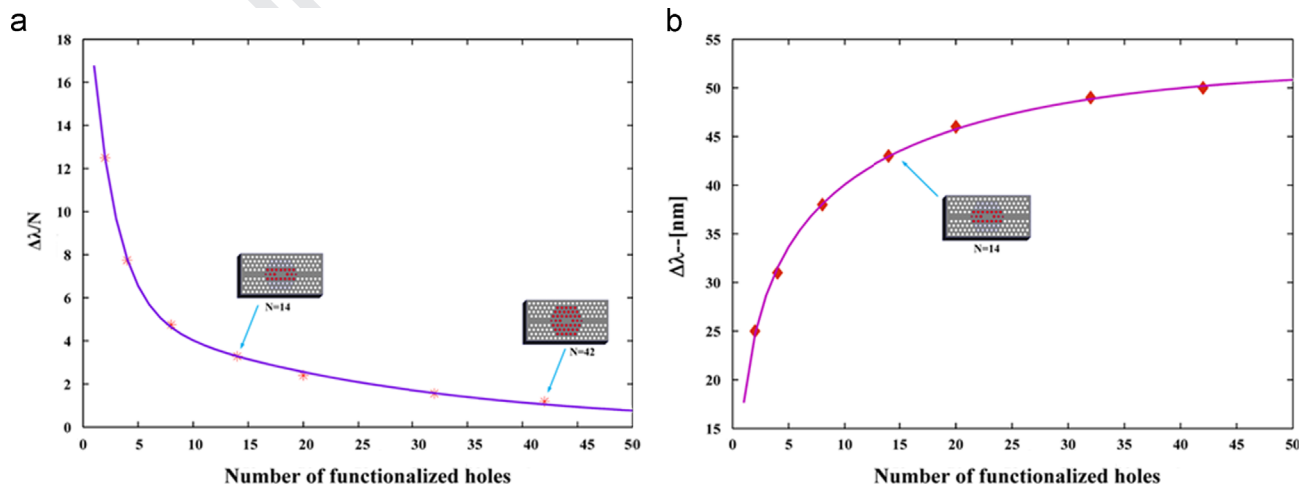


Fig. 10. (a) 3D-FDTD simulation showing the mass sensitivity of the device plotted as a function of the number of the functionalized holes. The orange solid star points indicate the sensitivity values calculated from the simulations. The purple curve shows a least-square fit using an analytical model for the device sensitivity which is described above, and (b) plot illustrating the dependence of the shift in resonant wavelength of a resonator on the number of functionalized holes. The deep yellow diamond holes indicate the data obtained from 3D-FDTD simulations. The pink curve is a best-fit curve of the form where a , b and c are arbitrary constants. The values of a , b , and c used here are 10.4341, -0.0877 , and 17.4780, respectively. (For interpretation of the references to color in this figure legend, the reader is referred to the web version of this article).

sensing element can realize higher refractive index sensitivity (Fig. 10(b), $N=20, 32$ and 42), but the mass sensitivity is lower. It is a tradeoff between the mass sensitivity and the refractive index sensitivity. So it is very important to choose the functionalized hole number ($N=14$) in our sensor design structure.

Through the design and discussion about the integration of broadband W1 waveguide and high transmittance H2 PhC nanocavity in above sections, it is noteworthy that this H2-type nanocavity can be used for measurement of solution concentrations. As seen in Fig. 8(c), the H2 PhC nanocavity contributes a sharp peak to the output spectrum of the device. We observe that this resonator possesses a large Q -factor (2966) and a full width at half maxima of less than a nanometer. This is important that higher Q -factors make it easier to detect very small shifts in the resonances. In this paper, in order to investigate the refractive index (RI) sensitivity of the device, different concentrations of sugar-water solutions with known refractive indices (Table 2) have been infiltrated into the optimal functionalized holes ($N=14$) around the cavity. Fig. 11 shows the typical response of the center cavity to eight different sugar-water concentrations. The resonance peak at 1546 nm was identified as pure water was infiltrated by using 3D-FDTD calculations. After sugar-water solutions are filled into, the resonant peak redshifts more than 20 nm due to the increase in the ambient refractive index from 1.33 to 1.53. In fact, using the combination of broadband W1 waveguide and high-performance H2 nanocavity, we can detect larger concentrations of sugar-water solutions with wide dynamic range. Therefore it is a meaningful way to produce different concentrations of sugar-water solutions as accurate as possible in industry.

Here in order to quantitatively analyze the RI sensitivity of the designed structure, we choose the sensitivity of our structure by observing the resonant wavelength shifts ($\Delta\lambda$) as a function of the variations in the refractive index (Δn). The RI sensitivity is expressed as following:

$$S = \Delta\lambda / \Delta n \quad (3)$$

As shown in Fig. 12, the device exhibits a bulk refractive index sensitivity that equals 131.70 nm/RIU. We also calculate the standard deviation and p -value by the statistic method to evaluate the bulk refractive index sensitivity. The standard deviation (σ) gives an idea of how close the entire set of data is to the fitting value. Data sets with a small standard deviation have tightly

Table 2
Refractive index (RI) and resonant wavelength change ($\Delta\lambda$) with different sugar–water solution concentration (C (%)).

C (%)	0	11	23	38	48	53	55	56	58	59	60
RI	1.33	1.35	1.37	1.39	1.41	1.43	1.45	1.47	1.49	1.51	1.53
$\Delta\lambda$	0	3	6	8	10	13	16	18	21	23	26

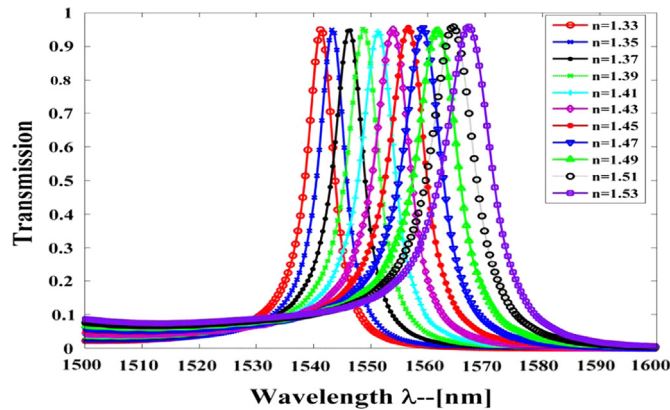


Fig. 11. Resonant wavelength change of the resonant cavity as the sugar concentration in the sugar–water solution increases (the refractive index is larger as the sugar–water solution concentration increases).

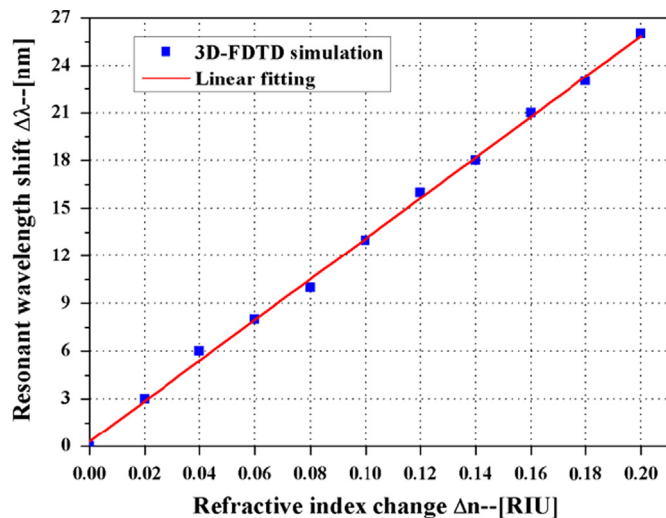


Fig. 12. Resonant wavelength shifts as a function of the change in refractive index of the functionalized holes. The blue squares indicate the data obtained from 3D-FDTD simulations. The red line is a best-fit line. (For interpretation of the references to color in this figure legend, the reader is referred to the web version of this article).

grouped, precise data. Data sets with large standard deviations have data spread out over a wide range of values. The formula for standard deviation is given below as Eq. (4)

$$\sigma = \sqrt{\frac{1}{n-1} \sum_{i=1}^{i=n} (X_i - \bar{X})^2} \quad (4)$$

where n , X_i and \bar{X} represent the number of test samples, the calculated value of simulation results, the fitting value of regression curve, respectively. The standard deviation (σ) is 16.82. A p -value is a statistical value that details how much evidence there is to reject the most common explanation for the data set. It can be considered to be the probability of obtaining a result at least as extreme as the one observed, given that the null hypothesis is true. In chemical engineering, the p -value is often used to analyze marginal conditions of a system, in which case the p -value is the

probability that the null hypothesis is true. The method for finding the p -value is actually rather simple. First calculate the z -score and then look up its corresponding p -value using the standard normal table. The formula for z -score is given below as Eq. (5)

$$z = \frac{X - \bar{X}}{\sigma / \sqrt{n}} \quad (5)$$

where X , \bar{X} , σ and n represent the measured value, the fitting value, the standard deviation, the number of samples, respectively. So if the level of significance is 5%, the p -value can be calculated to be 0.89435. Compare the probability to the significance level (i.e. 5% or 0.05), this probability is greater than 0.05, the null hypothesis is true and the observed data is not significantly different than the random. Therefore, finally, we can obtain the sensitivity of 131.70 ± 16.82 nm/RIU. Assuming an advanced spectral resolution of 0.5 pm, we estimate the bulk refractive index detection limit approximately 3.797×10^{-6} . Compared with techniques like SPR, the refractive index detection limit is not better. But it is able to drastically confine the detection volume by targeting the holes (especially the innermost holes as shown in simulations) thus allowing us to lower the mass limit of detection.

4. Conclusion

In this work we have proposed a new biosensor platform, which is an integration of high transmittance H2-type nanocavity and broadband W1 waveguide on SOI substrate. Characteristics based on the structure design have been demonstrated by numerical simulations. Simulation results show that the cavity with shrinking air holes and changing the length of defect in the waveguide confine at resonance and enhance the quality factor of the cavity. While obtaining the high transmission (over 95%), high extinction ratio (about 25 dB) and higher Q factor simultaneously by reducing unwanted reflection due to mismatch and minimization of propagation losses. Our simulation results also suggest the sensitivity equals 131.70 nm/RIU and a bulk refractive index resolution detection limit approximately 3.797×10^{-6} . In addition, through modifying the number of functionalized holes, the sensitivity can also range from 75.08 nm/RIU ($N=2$) to 150.15 nm/RIU ($N=42$). We believe that the results of this work will be valuable for understanding the influence of the design parameters on PC biosensor performance, and for designing highly sensitive, robust and large-range measured PC biosensors. Furthermore, the results are invaluable for the optimization of other PC applications, including optical filters, nanomechanical sensors, and enhanced-fluorescence biosensors.

Uncited reference

[34]

Acknowledgements

This research was supported by National Natural Science Foundation of China (no. 61372038), National 973 Program (no. 2012CB315705), National 863 Program (no. 2011AA010305), Post-graduate Innovation Fund of SICE, BUPT, 2013 and Fund of State

1 Key Laboratory of Information Photonics and Optical Communica-
 2 tions (Beijing University of Posts and Telecommunications),
 3 PR China.

4 References

- 5
6
7 [1] J.B. Jensen, L.H. Pedersen, P.E. Hoiby, L.B. Nielsen, T.P. Hansen, J.R. Folkenberg,
8 J. Riishede, D. Noordegraaf, K. Nielsen, A. Carlsen, A. Bjarklev, *Opt. Lett.* 29
9 (2004) 1974.
10 [2] E. Yablonovitch, *Phys. Rev. Lett.* 58 (1987) 2059.
11 [3] S. John, *Phys. Rev. Lett.* 58 (1987) 2486.
12 [4] W.C. Lai, S. Chakravarty, Y. Zou, R.T. Chen, *Opt. Lett.* 37 (2012) 1208.
13 [5] D. Yang, H. Tian, Y. Ji, *Opt. Express* 19 (2011) 20023.
14 [6] Y. Yang, D. Yang, H. Tian, Y. Ji, *Sens. Actuators A: Phys.* 193 (2013) 149.
15 [7] D. Yang, H. Tian, N. Wu, Y. Yang, Y. Ji, *Sens. Actuators A: Phys.* 199 (2013) 30.
16 [8] J.O. Grepstad, P. Kaspar, O. Solgaard, I.R. Johansen, A.S. Sudbø, *Opt. Express* 20
17 (2012) 7954.
18 [9] X. Sun, J. Zheng, M. Poot, C.W. Wong, H.X. Tang, *Nano Lett.* 12 (2012) 2299.
19 [10] S.H. Kwon, T. Sünner, M. Kamp, A. Forchel, *Opt. Express* 16 (2008) 11709.
20 [11] V. Trivino, N. Rossbach, G. Dharanipathy, U. Levrat, J. Castiglia, A. Carlin, J.
21 F. Atlasov, K.A. Butte, R. Houdre, R. Grandjean, *Appl. Phys. Lett.* 100 (2012)
22 071103.
23 [12] A. Faraon, C. Santori, Z. Huang, V.M. Acosta, R.G. Beausoleil, *Phys. Rev. Lett.* 109
24 (2012) 3604.
25 [13] T. Tawara, H. Kamada, T. Tanabe, T. Sogawa, P. Yao, P.K. Pathak, S. Hughes, *Opt.*
26 *Express* 18 (3) (2010) 2719.
[14] T. Sar, J. Hagemeyer, W. Pfaff, E. Heeres, S. Thon, H. Kim, P. Petroff, O. Tjerk,
D. Bouwmeester, R. Hanson, *J. Opt. Soc. Am. B* 29 (2012) 698.
[15] B.T. Tung, D.V. Dao, T. Ikeda, Y. Kanamori, K. Hane, Susumu Sugiyama, *Opt.*
Express 19 (2011) 8821.
[16] X. Gan, R.J. Shiue, Y. Gao, K.F. Mak, X. Yao, L. Li, A. Szep, D. Walker, J.J. Hone, T.
F. Heinz, D. Englund, *Nano Lett.* 13 (2013) 691.
[17] F. Tian, G. Zhou, Y. Du, F.S. Chau, J. Deng, R. Akkipeddi, *Opt. Lett.* 38 (2013)
2005.
[18] F. Ouerghi, F. AbdelMalek, S. Haxha, E.K. Akowuah, H. Ademgil, *J. Lightwave*
Technol. 30 (2012) 3288.
[19] M. Larqué, T. Karle, I. Robert-Philip, A. Beveratos, *New J. Phys.* 11 (2009)
033022.
[20] J.L. Dominguez-Juarez, G. Kozyreff, J. Martorell, *Nat. Commun.* 2 (2011) 1.
[21] P. Alivisatos, *Nat. Biotechnol.* 22 (2004) 47.
[22] H. Kurt, M.N. Erim, N. Erim, *Sens. Actuators A: Phys.* 165 (2012) 68.
[23] M.A. Dündar, E.C.I. Ryckebosch, R. Notzel, F. Karouta, L.J. van Ijzendoorn, R.
W. van der Heijden, *Opt. Express* 18 (2010) 4049.
[24] C. Monat, P. Domachuk, B.J. Eggleton, *Nat. Photon.* 1 (2007) 106.
[25] A. Chutinan, S. Noda, *Phys. Rev. B* 62 (2000) 4488.
[26] K. Inoue, H. Oda, N. Ikeda, K. Asakawa, *Opt. Express* 17 (2009) 7206.
[27] J. Joannopoulos, R. Meade, J. Winn, *Photonic Crystals: Molding the Flow of*
Light, Princeton University Press, Princeton, 1995.
[28] O. Painter, J. Vučković, A. Scherer, *J. Opt. Soc. Am. B* 16 (1999) 275.
[29] Steven G. Johnson, Shanhui Fan, Pierre R. Villeneuve, J.D. Joannopoulos, *Phys.*
Rev. B 60 (1999) 5751.
[30] S. Haddadi, L. Le-Gratiet, I. Sagnes, F. Raineri, A. Bazin, K. Bencheikh, J.
A. Levenson, A.M. Yacomotti, *Opt. Express* 20 (2012) 18876.
[31] H. Lu, X. Liu, Y. Gong, D. Mao, L. Wang, *Opt. Express* 19 (2011) 12885.
[32] Y. Akahane, T. Asano, B.S. Song, S. Noda, *Nature* 425 (2003) 944.
[33] R. Shankar, R. Leijssen, I. Bulu, M. Lončar, *Opt. Express* 19 (2011) 5579.
[34] K.J. Vahala, *Nature* 424 (2003) 839.
[35] H. Takagi, Y. Ota, N. Kumagai, S. Ishida, S. Iwamoto, Y. Arakawa, *Opt. Express* 20
(2012) 28292.
[36] J.D. Joannopoulos, S.G. Johnson, J.N. Winn, R.D. Meade, *Photonic Crystals,*
Molding the Flow of Light Princeton, University Press, 2007.
[37] S.Y. Lin, E. Chow, S.G. Johnson, J.D. Joannopoulos, *Opt. Lett.* 26 (2001) 1903.